AGU PUBLICATIONS

JGR

Journal of Geophysical Research: Space Physics

RESEARCH ARTICLE
10.1002/2016JA022365

Slow electrostatic solitary waves in Earth's plasma sheet boundary layer

Amar Kakad[1], Bharati Kakad[1], Chandrasekhar Anekallu[2], Gurbax Lakhina[1], Yoshiharu Omura[3], and Andrew Fazakerley[2]

[1]Indian Institute of Geomagnetism, New Panvel, Navi Mumbai, India, [2]Mullard Space Science Laboratory, University College London, London, UK, [3]Research Institute for Sustainable Humanosphere, Kyoto University, Kyoto, Japan

Key Points:
- Slow electrostatic solitary waves observed by Cluster in the plasma sheet boundary layer
- The wave observations modeled by nonlinear fluid theory and fluid simulation
- The study suggest that the slow solitary waves can be explained by slow ion acoustic solitary waves

Correspondence to:
A. Kakad,
amar@iigs.iigm.res.in

Citation:
Kakad, A., B. Kakad, C. Anekallu, G. Lakhina, Y. Omura, and A. Fazakerley (2016), Slow electrostatic solitary waves in Earth's plasma sheet boundary layer, *J. Geophys. Res. Space Physics*, *121*, doi:10.1002/2016JA022365.

Received 11 JAN 2016
Accepted 27 APR 2016
Accepted article online 4 MAY 2016

Abstract We modeled Cluster spacecraft observations of slow electrostatic solitary waves (SESWs) in the Earth's northern plasma sheet boundary layer (PSBL) region on the basis of nonlinear fluid theory and fluid simulation. Various plasma parameters observed by the Cluster satellite at the time of the SESWs were examined to investigate the generation process of the SESWs. The nonlinear fluid model shows the coexistence of slow and fast ion acoustic waves and the presence of electron acoustic waves in the PSBL region. The fluid simulations, performed to examine the evolution of these waves in the PSBL region, showed the presence of an extra mode along with the waves supported by the nonlinear fluid theory. This extra mode is identified as the Buneman mode, which is generated by relative drifts of ions and electrons. A detailed investigation of the characteristics of the SESWs reveals that the SESWs are slow ion acoustic solitary waves.

1. Introduction

Electrostatic solitary waves (ESWs) are ubiquitous in space plasmas and are manifestations of highly nonlinear processes. For a long time, before it became customary to sample waveforms captured by the Geotail spacecraft in the Earth's plasma sheet boundary layer (PSBL), they were often interpreted as broadband electrostatic noise. Subsequently, they were identified as sequences of electrostatic impulsive solitary waves in electric field data [*Matsumoto et al.*, 1994]. ESWs have since been observed in many different plasma settings, including space [*Ergun et al.*, 1998; *Bale et al.*, 1998; *Mangeney et al.*, 1999; *Cattell et al.*, 2002; *Matsumoto et al.*, 2003; *Pickett et al.*, 2005; *Wilson et al.*, 2010; *Malaspina et al.*, 2013] and laboratory plasmas [*Pickett et al.*, 2009; *Lefebvre et al.*, 2010, 2011; *Fox et al.*, 2012]. Moreover, many theoretical and numerical studies have been carried out to examine the generation of ESWs under various conditions [*Omura et al.*, 1996; *Goldman et al.*, 1999; *Chen et al.*, 2004; *Kakad et al.*, 2007; *Lakhina et al.*, 2008a, 2008b, 2009, 2011; *Kakad et al.*, 2013].

ESWs are small-scale structures representing holes in the electron/ion phase space or density enhancements and depletions, depending on whether they are Bernstein-Greene-Kruskal structures generated by a beam, two-stream, or kinetic Buneman type of instability [*Bernstein et al.*, 1957; *Omura et al.*, 1996; *Goldman et al.*, 1999; *Chen et al.*, 2004] or an electron/ion acoustic mode generated by an electron/ion acoustic instability [*Dubouloz et al.*, 1993; *Berthomier et al.*, 1998; *Kakad et al.*, 2007; *Lakhina et al.*, 2009, 2011; *Kakad et al.*, 2013, 2014]. They have been observed in the Earth's magnetotail by several spacecraft missions, first and most notably by Geotail [*Matsumoto et al.*, 1994] in the far tail, followed by Polar [*Cattell et al.*, 1999; *Franz et al.*, 1998] in the near-Earth plasma sheet and by Cluster in the midtail plasma sheet [*Pickett et al.*, 2004]. ESWs have also been observed in association with reconnection in the magnetotail [*Li et al.*, 2014] and in association with high-speed flows along the magnetic field in the PSBL region [*Kojima et al.*, 1994; *Lakhina et al.*, 2011].

Norgren et al. [2015a] reported Cluster multispacecraft observations of slow electrostatic solitary waves (SESWs) in the PSBL, moving earthward with a speed close to 500 km s^{-1} with respect to the spacecraft frame of reference. Low-energy electrons drifting along the magnetic field were observed simultaneously with SESWs, and they were speculated to be responsible for the generation of the SESWs through the Buneman instability. The authors interpreted the SESWs as slow electron holes generated through the Buneman instability. While their study suggested that electrons with a bulk drift velocity of ~7000 km s^{-1} are required for the Buneman instability, such high electron bulk flows were not observed by Cluster during the SESW event. Thus, the suggestion that SESWs occur through the Buneman instability is not satisfactory. In the current study, we attempted to model these SESWs on the basis of the nonlinear fluid theory and fluid simulation.

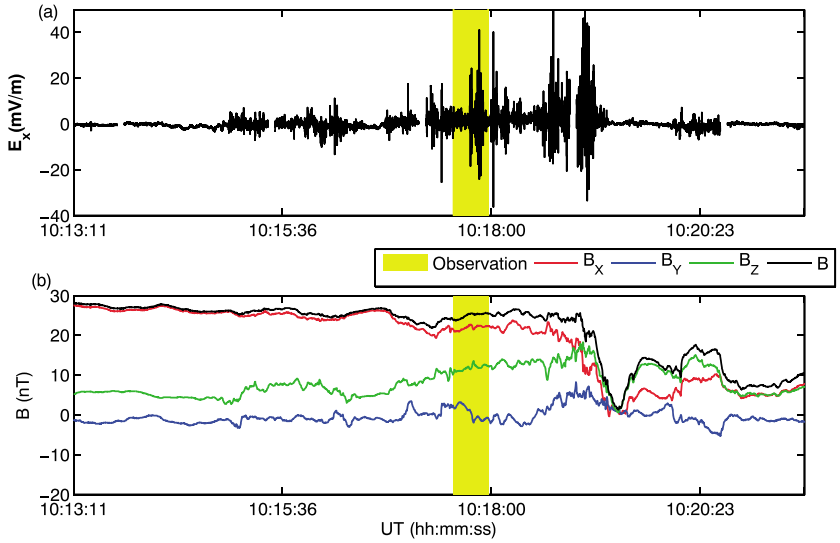

Figure 1. (a) Electric and (b) magnetic field observations of C4 on 31 August 2007. The electric field structures observed from 10:17:33.6 to 10:17:58.2 UT (shown by yellow patch) were considered in this study.

We observe a strong association between the plasma population and the observed SESWs in the Earth's PSBL. Furthermore, the half width, speed, and amplitude of the observed SESWs are in excellent agreement with those obtained from the theory and simulation, suggesting that the observed SESWs correspond to the slow ion acoustic mode. This paper is organized as follows. In section 2, Cluster observations of SESWs and the plasma characteristics in the PSBL are presented, and in section 3, the nonlinear fluid model is discussed. The application of the model to the SESW observations is briefly described in section 4, and fluid simulations of SESWs are discussed in section 5. Finally, the present work is summarized and concluded in section 6.

2. Observations

We use Cluster spacecraft measurements of ESWs and ambient plasma characteristics of a PSBL interval from 31 August 2007. We use data from Electric Field and Wave experiment [*Gustafsson et al.*, 1997] on board Cluster-3 (C3) and Cluster-4 (C4) spacecraft and electron and ion observations from Plasma Electron and Current Experiment (PEACE) [*Johnstone et al.*, 1997] and Hot Ion Analyzer (HIA) [*Réme et al.*, 1997] payloads on board Cluster-3. The characteristic speeds of these ESWs were found to be less than the thermal velocity of the electrons. Hence, *Norgren et al.* [2015a] termed these ESWs as slow ESWs. We study this SESW event in the PSBL, during which Cluster spacecraft was in Earth's magnetotail at about (−14, −4, 2) R_E in geocentric solar magnetospheric (GSM) coordinates. During this interval C3 and C4 were separated only by 40 km and PEACE instruments are in burst mode and are collecting high time resolution data.

Figure 1 shows the electric (a) and magnetic (b) field observations from 31 August 2007. An increased activity is observed in electric field at both C3 and C4 during 10:15–10:19 UT. *Norgren et al.* [2015a] interpreted electric field structures observed during 10:17:33.600–10:17:58.200 UT, highlighted in yellow, as a series of slow electron holes, whereas the large-amplitude electric fields encountered during 10:18:25–10:19:26, present at the sharpest magnetic field gradient (Figure 1b), are interpreted as lower hybrid waves [*Norgren et al.*, 2012]. Detailed description of the spacecraft crossing and SESW event is presented in *Norgren et al.* [2015a].

A scrutiny of the electric field observations from the C3 and C4 spacecraft at around 10:17:35 to 10:17:58 UT shows a series of short-duration bipolar pulses, which are shown in Figure 2a. In these electric field pulses, the positive polarity is followed by the negative polarity in the spacecraft reference frame. Moreover, the bipolar electric field pulses are first observed on C4 and then on C3 (C4 is located tailward of C3), implying that the structures are traveling parallel to the magnetic field, which in this case is directed earthward. The vertical dash-dotted lines in Figure 2a show two earthward propagating SESWs. The intervals are shown in Figures 2b and 2c on an expanded scale. Overall, 10 SESWs with drift speeds of approximately 350–800 km/s, half widths of 4–7 km, and amplitudes of 10–30 mV/m were reported during this event [*Norgren et al.*, 2015a]. The observed speed, half width, and amplitude of one of the SESWs were 440 km/s, 7 km, and 17–26 mV/m,

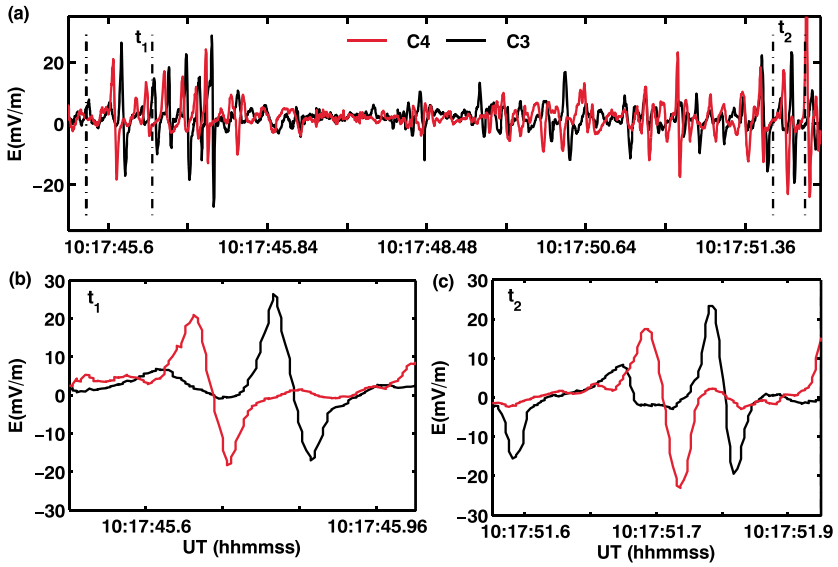

Figure 2. (a) Electric field observed by the C3 and C4 spacecraft during the interval 10:17:35 to 10:17:58 UT. The vertical dash-dotted lines in Figure 2a mark the two (t_1 and t_2) earthward propagating SESWs. (b and c) Magnified view of electric pulses.

and those of the other SESWs were 380 km/s, 4 km, and 17–24 mV/m. In the current study, we modeled the two SESWs observed at the time instants t_1 and t_2 shown in Figure 2.

We analyzed the plasma composition and plasma characteristics during the aforementioned event to determine the plasma mode supporting the generation of the SESWs. As the CIS-HIA instrument on board C4 was not operational beyond 2001, we use plasma data from C3. Furthermore, as C3 and C4 were only 40 km apart, it is reasonable to expect that the plasma composition at the locations of both spacecraft will be identical. For a considerable difference in the plasma composition, the bipolar electric field pulses should have been strongly modified during propagation from C4 to C3. Figure 3 shows the detailed plasma characteristics observed by the C3 spacecraft during the SESWs. Figures 3a and 3b show the observed electron and ion differential fluxes, respectively, for the period 10:12 to 10:26 UT. We computed the density, velocity, and temperature of the electrons and ions by using the moments of the electron and ion distribution functions [*Paschmann et al.*, 1998]. On the basis of their thermal energies, the electrons and ions were separated into low- and high-energy populations. The low-energy populations (with energies less than 250 eV) are termed "cold," and the high-energy populations (with energies greater than 250 eV) are termed "hot." With this criteria, the density, velocity, and temperature of the electrons are shown in Figures 3c, 3e, and 3g, respectively, and those of the ions are shown in Figures 3d, 3f, and 3h, respectively. The time when SESWs were observed is marked by a black rectangle in Figure 3. The calculated moments of the electron and ion distribution functions revealed the presence of both cold and hot electrons and ions in the Earth's PSBL region during the SESW event.

The estimated ambient plasma parameters are listed in Table 1. The positions of the C3 and C4 spacecraft, directions of SESWs, and the particle beams in the northern PSBL region are shown schematically in Figure 4. Cold and hot counterstreaming electrons and ions can be clearly seen during the SESW event. The hot electrons and ions show earthward motion, similar to the bipolar electric field structures. The cold ion population shows a negligible drift speed, and their direction of motion is not clear. The cold electrons show tailward motion, which is opposite to the direction of motion of the bipolar electric field structure. On the basis of these observations, we constructed a nonlinear fluid model for the observed bipolar electric field structures.

3. Theoretical Model

We modeled the Earth's PSBL region plasma as an infinite, collisionless, and magnetized plasma system consisting of cold electrons, hot electrons, cold ions, and hot ions. In the Earth's PSBL region, the dominant ion species is hydrogen (protons). Therefore, in the model, the plasma was considered to consist of electrons and protons. We treated all the species as mobile and considered only nonlinear electrostatic waves

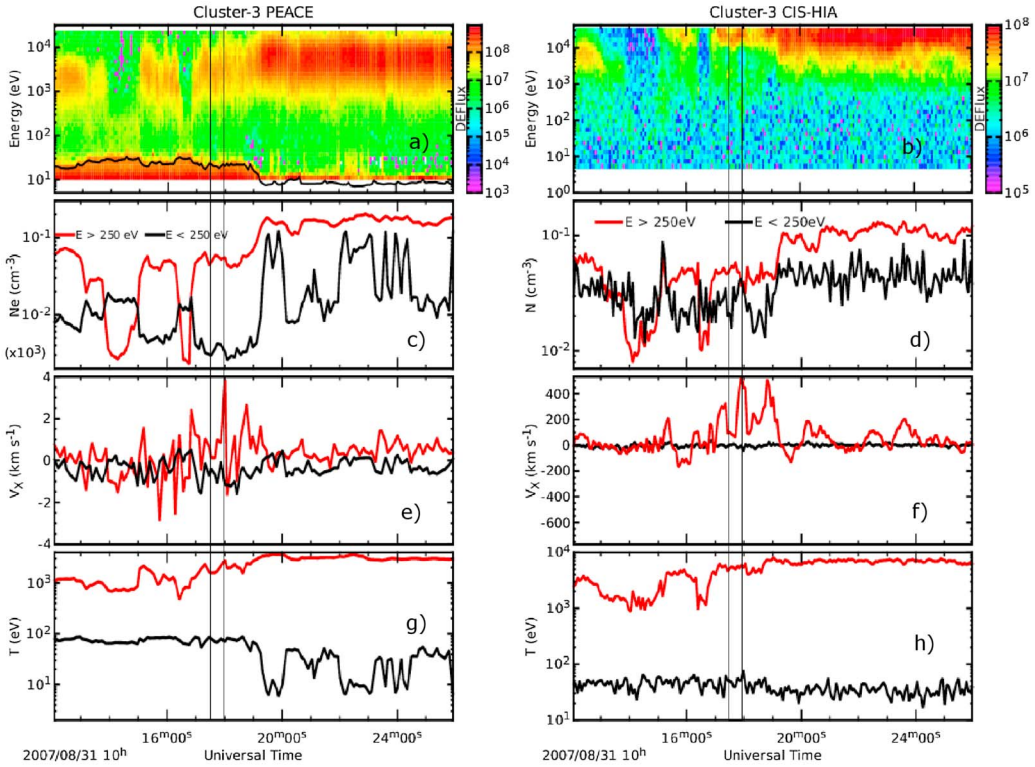

Figure 3. Cluster-3 (C3) observations in the northern PSBL. (a) Electron differential flux from PEACE. (b) Ion differential flux from CIS/HIA. The density, velocity, and temperature of the electrons and ions were computed by using the moments of the electron and ion distribution functions. The (c) density, (e) velocity, and (g) temperature of the cold and hot electrons are shown. The (d) density, (f) velocity, and (h) temperature of the cold and hot ions are presented. The black line in Figure 3a shows the spacecraft potential. The SESWs were observed during the interval between the two vertical lines.

propagating parallel to the magnetic field. Therefore, the dynamics of each species was governed by the multifluid equations of continuity, momentum, and equation of state, and the Poisson equation [*Lakhina et al.*, 2009].

$$\frac{\partial n_j}{\partial t} + \frac{\partial (n_j v_j)}{\partial x} = 0 \tag{1}$$

$$\frac{\partial v_j}{\partial t} + v_j \frac{\partial v_j}{\partial x} + \frac{1}{\mu_j n_j} \frac{\partial P_j}{\partial x} + \frac{Z_j}{\mu_j} \frac{\partial \phi}{\partial x} = 0 \tag{2}$$

$$\frac{\partial P_j}{\partial t} + v_j \frac{\partial P_j}{\partial x} + \gamma_j P_j \frac{\partial v_j}{\partial x} = 0 \tag{3}$$

Table 1. Cluster-3 Observations of Electrons and Ions in the Earth's Northern PSBL Region

Observation	Time	Cold Electrons			Hot Electrons			Cold Ions			Hot Ions		
No.	(hhmmss)	N_{ce} (/cc)	v_{ce} (km/s)	T_{ce} (eV)	N_{he} (/cc)	v_{he} (km/s)	T_{he} (eV)	N_{ci} (/cc)	v_{ci} (km/s)	T_{ci} (eV)	N_{hi} (/cc)	v_{hi} (km/s)	T_{hi} (eV)
Obs. 1	101737	0.003	−590	73	0.055	124	1587	0.036	11	40	0.053	75	5311
Obs. 2	101742	0.004	−837	69	0.058	447	1630	0.027	1	40	0.059	64	4954
Obs. 3	101746	0.004	−907	70	0.057	968	1790	0.031	−20	56	0.048	290	5654
Obs. 4	101750	0.004	−381	76	0.054	889	2034	0.041	−15	51	0.048	445	5225
Obs. 5	101754	0.004	−267	78	0.053	1423	2299	0.042	−2	52	0.036	534	5841
Obs. 6	101758	0.004	−824	74	0.054	2941	2595	0.034	−48	78	0.040	449	5338

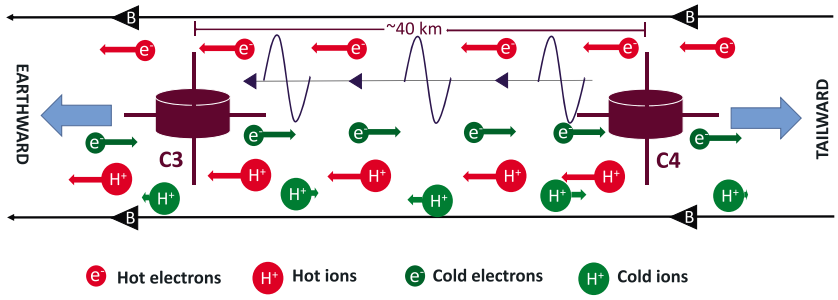

Figure 4. Schematic of the ambient plasma parameters observed by the C3 and C4 spacecraft in the northern PSBL region.

$$\frac{\partial^2 \phi}{\partial x^2} = n_{ce} + n_{he} - n_{ci} - n_{hi} \tag{4}$$

Here the normalized quantities n_j, v_j, and P_j denote the number density, fluid velocity, and pressure of species j, respectively. The indices ($j =$)ce, he, ci, and hi denote cold electron, hot electron, cold proton, and hot proton species, respectively. The normalized wave potential is given by ϕ, and the normalized mass of species j is given by $\mu_j = m_j/m_i$, where m_j is the mass of species j and m_i is the proton mass. The charge of species j is denoted by Z_j, with $Z_{ci} = Z_{hi} = 1$ and $Z_{ce} = Z_{he} = -1$. All densities are normalized with respect to the total equilibrium (unnormalized) ion number density $N^0 = N^0_{ci} + N^0_{hi}$. From the charge neutrality at equilibrium, the normalized equilibrium densities follow $n^0_{ce} + n^0_{he} = n^0_{ci} + n^0_{hi} = 1$. Velocities are normalized with respect to the hot ion thermal speed, given by $v_{\text{thi}} = (k_B T_{hi}/m_i)^{1/2}$. Here k_B is the Boltzmann constant. The time and lengths are normalized by the inverse of the ion plasma frequency, expressed as $\omega_{pi}^{-1} = (m_i \epsilon_0/N^0 e^2)^{1/2}$, and the ion Debye length, given by $\lambda_{di} = (\epsilon_0 k_B T_{hi}/N^0 e^2)^{1/2}$, respectively. The potential ϕ is normalized with respect to $k_B T_{hi}/e$, while the pressure P_j is normalized with respect to $N^0 k_B T_{hi}$.

We performed the Sagdeev pseudopotential analysis, which retains the full complexity of the nonlinearity, to obtain arbitrary solitary wave solutions. The analysis involved the construction of Sagdeev potentials in a moving frame of reference, which was given by

$$\xi = x - Mt \tag{5}$$

Furthermore, we have $M = V/v_{\text{thi}}$, where V is the speed of the solitary wave and v_{thi} is the thermal speed of the hot ions.

The number density of each species j and the electrostatic potential ϕ satisfy the boundary conditions $n_j \to n^0_j$ and $\phi \to 0$ when $\xi \to \pm\infty$. For each inertial species j, we also imposed the boundary conditions $v_j \to v_{j0}$ and $P_j \to k_B n^0_j T_j$ when $\xi \to \pm\infty$. Using equation (5) in equations (1)–(3) and solving them yield an expression for the number density of each species [*Olivier et al.*, 2015].

$$n_j = \frac{n^0_j}{2B_j}\left[\left(A^2_{j+} - \frac{2Z_j\phi}{\mu_j}\right)^{\frac{1}{2}}\right] \pm \left[\left(A^2_{j-} - \frac{2Z_j\phi}{\mu_j}\right)^{\frac{1}{2}}\right] \tag{6}$$

At equilibrium, $\phi = 0$ gives $n_j = n^0_j$ that satisfies the quasi-neutrality condition. Here $A_{j\pm} = M - v_j \pm B_j$ and $B_j = \sqrt{3T_j/\mu_j}$ for the $j = ce, he, ci$, and hi. For the one-dimensional case, we consider the polytropic index $\gamma_j = 3$ in this model.

In studying solitary structures propagating in multispecies plasmas, one may define plasma species as being "high" thermal speed species, i.e., the solitary wave structure speed is less than the species thermal speed, $V < v_{\text{thj}}$, or "low" thermal speed species, $V > v_{\text{thj}}$ [*Verheest et al.*, 2004]. Since $n_j = n^0_j$ at equilibrium, it follows that the solutions with plus and minus signs correspond to high thermal speed ($M - v_{0j} < B_j$) and low thermal speed species ($M - v_{0j} > B_j$), respectively [*Olivier et al.*, 2015]. The different signs can be inconvenient when

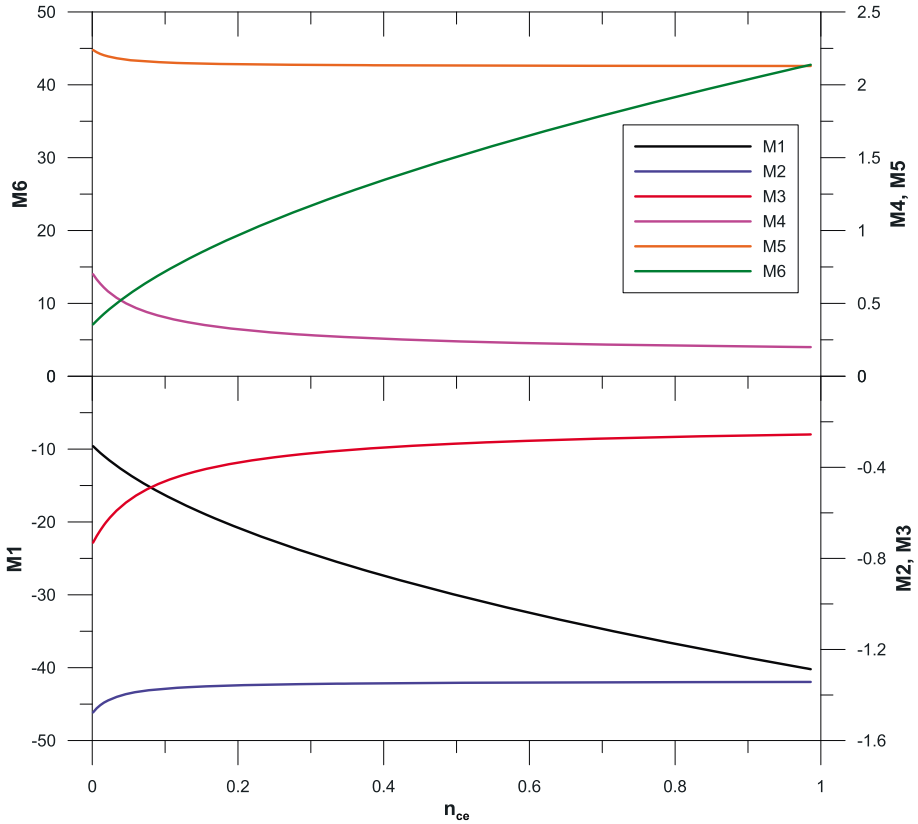

Figure 5. Variation of the Mach number with the cold electron density n_{ce} for Obs. 3. Among the six roots, the Mach number *M*4 is associated with the earthward propagating slow ion acoustic waves.

considering both high and low thermal speed species. This sign ambiguity can be removed by taking A_j^2 out of the square root terms in equation (6). The number density of species *j* can then be written as [*Olivier et al.*, 2015]

$$n_j = \frac{n_j^0 A_{j+}}{2B_j}\left(1 - \frac{2Z_j\phi}{\mu_j A_{j+}^2}\right)^{\frac{1}{2}} - \frac{n_j^0 A_{j-}}{2B_j}\left(1 - \frac{2Z_j\phi}{\mu_j A_{j-}^2}\right)^{\frac{1}{2}} \tag{7}$$

The advantage of using this form of the density expression is that it applies to both high and low thermal speed species in the model. Substituting the expressions for the number densities into Poisson's equation (equation (4)) for all four species and integrating Poissons equation give the following energy integral:

$$\frac{1}{2}\left(\frac{\partial\phi}{\partial\xi}\right)^2 + S(\phi, M) = 0 \tag{8}$$

where

$$S(\phi, M) = \sum_j \frac{\mu_j n_j^0 A_{j+}^3}{6B_j}\left[1 - \left(1 - \frac{2Z_j\phi}{\mu_j A_{j+}^2}\right)^{\frac{3}{2}}\right] - \sum_j \frac{\mu_j n_j^0 A_{j-}^3}{6B_j}\left[1 - \left(1 - \frac{2Z_j\phi}{\mu_j A_{j-}^2}\right)^{\frac{3}{2}}\right] \tag{9}$$

Equation (8) yields solitary wave solution when the Sagdeev potential $S(\phi, M)$ satisfies the following conditions: $S(\phi, M) = 0, dS(\phi, M)/d\phi = 0, d^2S(\phi, M)/d\phi^2 < 0$ at $\phi = 0$; $S(\phi, M) = 0$ at $\phi = \phi_{max}$, and $S(\phi, M) < 0$ for $0 <| \phi |<| \phi_{max} |$. When these conditions are satisfied, the pseudoparticle is reflected in the pseudopotential field and returns to its initial state (zero potential drop) for the solitary wave solution.

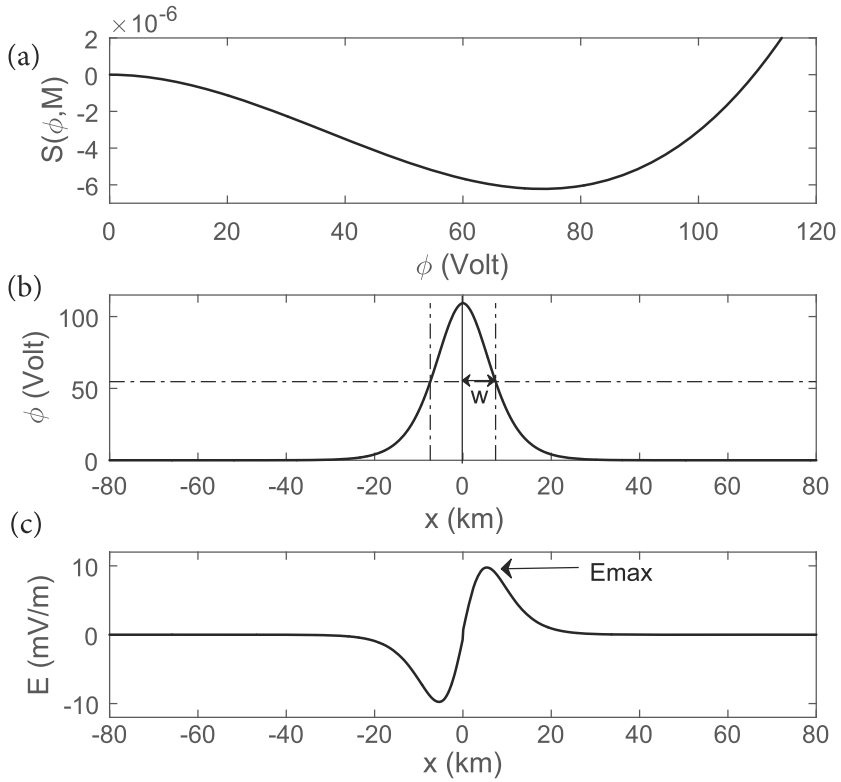

Figure 6. (a) Variation of the Sagdeev pseudopotential $S(\phi, M)$ with the electrostatic potential ϕ for slow ion acoustic solitary waves for the parameters of Figure 5. The Sagdeev potential profile is associated with one of the Mach numbers of the slow ion acoustic waves, $M = 0.5746$ (corresponding to a hot ion beam velocity of 410 km/s), and $n_{ce} = 0.2\%$. (b and c) The associated electrostatic potential and electric field of the slow ion acoustic solitary waves are shown.

In equation (9), it can be seen that $S(\phi, M)$ and its first derivative with respect to ϕ vanish at $\phi = 0$. The condition $d^2S(\phi, M)/d\phi^2 < 0$ at $\phi = 0$ is satisfied provided that $M > M_0$, where M_0 satisfies the equation

$$f(M_0) \equiv \sum_j \frac{n_j^0}{\mu_j \left[(M_0 - v_j)^2 - B_j \right]} = 0 \tag{10}$$

We solved equation (10) for the observed electron and ion parameters for the six events listed in Table 1. In our model, we considered quasi-neutrality at the equilibrium. It should be noted that the total ion density ($N_i = N_{ci} + N_{hi}$) and electron density ($N_e = N_{ce} + N_{he}$) differ slightly. To impose the quasi-neutrality assumption, we treated the cold electron density as a free parameter in the analysis . For any observation listed in Table 1 (i.e., Obs. 1 to Obs. 6), equation (10) gives six roots (i.e., Mach numbers). Each Mach number gives the velocity of a distinct solitary wave, whereas its sign represents the direction of wave propagation. As an example, in Figure 5, we show the variation of the Mach number as a function of the cold electron density for Obs. 3.

According to the propagation directions of electron and ion beams used in the model, positive Mach numbers indicate that the corresponding solitary waves propagate in the earthward direction, whereas negative Mach numbers show the tailward propagation of solitary waves. Among these Mach numbers, *M*1 and *M*6 are associated with the electron acoustic mode, *M*3 and *M*4 are related to slow ion acoustic waves, and *M*2 and *M*5 are associated with fast ion acoustic waves. For using this model to explain the slow solitary waves propagating earthward with a speed lesser than 500 km/s, we consider the root *M*4, which is associated with slow ion acoustic solitary waves propagating earthward. The roots corresponding to electron acoustic and fast ion acoustic waves would yield speeds greater than those of the SESWs, and therefore, they are not considered in the present study.

The Mach number *M*4 ranges from 0.25 to 0.75 for n_{ce} in the range 0–1. We chose $M = 0.5746$ (410 km s^{-1}), which corresponds to $n_{ce} = 0.002$, and obtained the Sagdeev pseudopotential $S(\phi, M)$ as a function of ϕ from

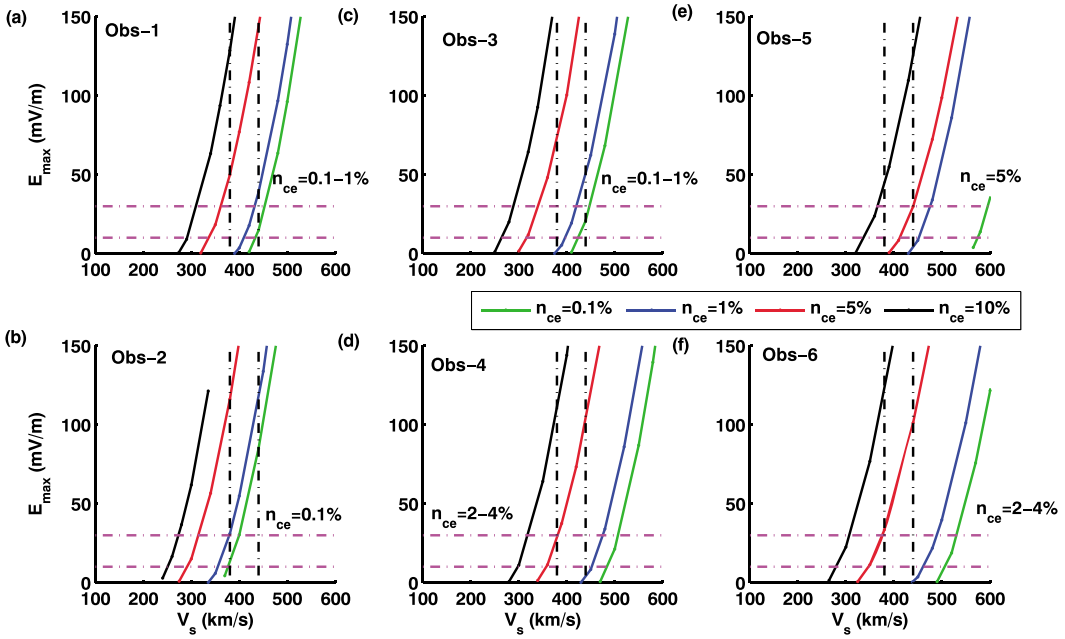

Figure 7. Variation of the maximum electric field with the phase speed for n_{ce} = 0.1, 1, 5, and 10% for the six observations listed in Table 1; Figures 7a–7f correspond to the observations in Table 1.

equation (9). The pseudopotential is shown in Figure 6a. This pseudopotential gives the boundary values, $\phi = 0$ and $\phi = \phi_{max}$, at which the $S(\phi, M)$ becomes zero. These boundary values restrict the pseudoparticle motion in the potential well between $0 < \phi < \phi_{max}$, which is an allowed part of the potential curve $S(\phi, M)$ (as shown in Figure 6a). Considering $\phi = \phi_{max}$ as the initial value, we solved the differential equation in equation (8) for the electrostatic potential ϕ and electric field (E) associated with the slow ion acoustic solitary wave. The unnormalized electrostatic potential and electric field are shown in Figures 6b and 6c, respectively. The amplitude of the solitary structure E_{max} and the half width at the half maximum, W, are also shown in these figures.

4. Application of the Model to SESW Observations

We obtained the characteristics of the slow ion acoustic mode from the nonlinear fluid model for Obs. 1 to Obs. 6 and compare them with those of the observed SESWs. For each set of observations listed in Table 1, we varied the cold electron density n_{ce} to have values of 0.1%, 1%, 5%, and 10% of the total electron density and ran the model to obtain the phase velocity (V_s), maximum electric field (E_{max}), and half width (W) of the bipolar electric field structures from equation (8).

Figure 7 shows the variation of the maximum electric field as a function of the phase velocity for the six observations in Table 1. Different curves correspond to different percentages of the cold electron density. The horizontal and vertical lines indicate the observed ranges of the maximum electric field E_{max} (10–30 mV/m) and phase speed V_s (380–440 km/s), respectively. The rectangular window formed by the vertical and horizontal lines represents the regime where the observed V_s and E_{max} of the SESWs match well with the model values. The range of the cold electron density for the theoretical curves covering the allowed observational window is specified in each subplot. Notably, curves corresponding to $n_{ce} \sim 0.1\%–1\%$ (2%–5%) mostly cover the observational window for Obs. 1–3 (observations 4–6). We also estimated the widths of the electric field structures obtained from the theoretical model. We chose the above-mentioned procedure to fit the observed widths and speeds with those obtained from the theoretical model. Figure 8 shows the variation of the half width (W) as a function of the phase speed (V_s) of the SESWs modeled for the six observations in Table 1. The curves corresponding to $n_{ce} \sim 0.1\%–1\%$ (2%–5%) accord with the observational window for Obs. 1–3 (Obs. 4–6).

The occurrence times t_1 and t_2 of two SESW observations shown in Figure 3 are close to those of Obs. 3 and Obs. 4, respectively. Therefore, we considered the plasma parameters for Obs. 3 and Obs. 4 and varied n_{ce}

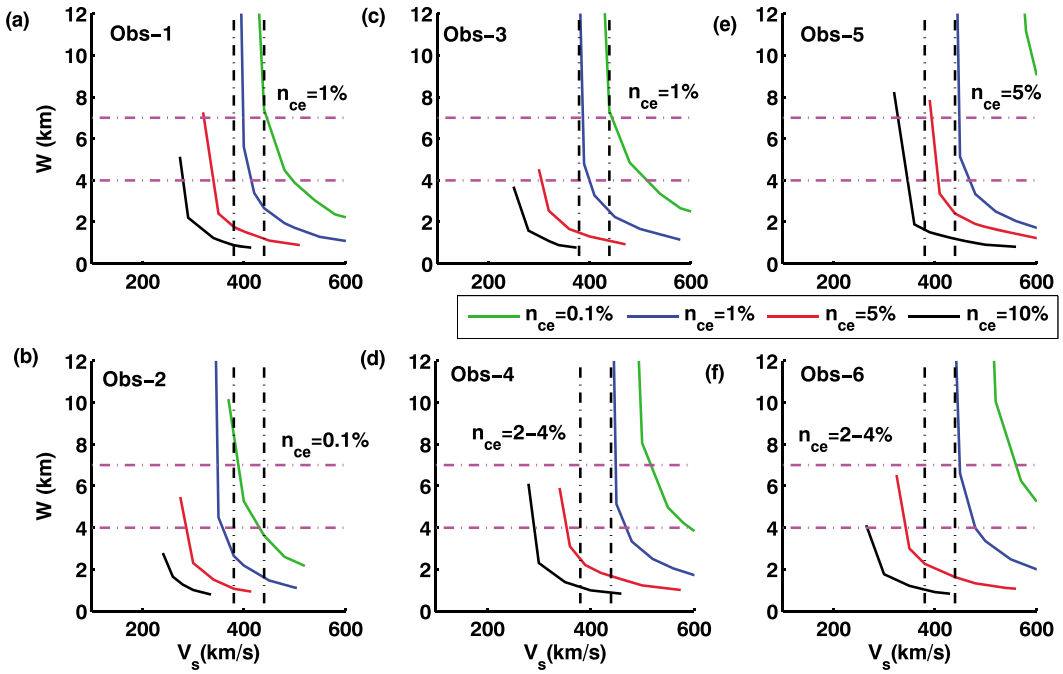

Figure 8. Width and phase speed of the bipolar electric field pulses associated with the slow ion acoustic waves for n_{ce} = 0.1, 1, 5, and 10% for the six observations listed in Table 1; Figures 8a–8f correspond to the observations in the table.

for modeling these two SESWs. The cold electron densities were chosen from density ranges obtained from Figures 7 and 8. We found that the electric field pulse obtained from the theoretical model for n_{ce} = 0.2% matched well with that observed at t_1, that is, 10:17:45:6 UT (shown in Figure 9a). The electric field pulse observed at time t_2, that is, 10:17:51:7 UT (shown in Figure 9b), is reproduced from the model by considering n_{ce} = 5%. Figures 9a and 9b indicate that the characteristics of the observed SESWs, such as the speed, half-width potential, and electric field amplitude, are in good agreement with those obtained from the nonlinear theoretical model. The required cold electron densities were found to be 0.2% and 5%, which corresponded to N_{ce} = 0.0002 and 0.004 cm^{-3}, respectively. The cold electron density observed by Cluster during the SESW event was in the range of 0.003–0.004 cm^{-3}. In particular, the cold electron density provided by the model for Obs. 3 is slightly lower than that observed by Cluster.

There is uncertainty in determining the cold electron density from the observations because of the data contamination due to spacecraft charge potential by photoelectrons. However, while determining the cold electron density, we took into account the cold electrons with the energies above the spacecraft potential that is shown with the black curve in Figure 2a. This generally provides somewhat accurate electron moment computation that eliminates contribution of photoelectrons but certainly will have some uncertainty. Therefore, we treated the cold electron density as a free parameter in the analysis. Nevertheless, we tried to speculate the required cold electron density to have SESWs with the observed characteristics in the PSBL region. Our analysis indicates that the 0.2% (5%) cold electron population can reproduce Obs. 3 (Obs. 4).

5. Fluid Simulation of SESWs

Cluster observations showed drifting populations of ions and electrons in the PSBL, indicating the possibility of excitation of beam instabilities in the plasma. The nonlinear fluid theory of the Sagdeev pseudopotential does not predict such instabilities in the plasma system. Therefore, the question arises; can SESWs such as slow ion acoustic waves propagate in the presence of beam instabilities? We performed a one-dimensional fluid simulation by considering the PSBL observations, for examining the evolution of slow ion acoustic waves in the presence of evolving beam instabilities for Obs. 4. In the development of the fluid code for the PSBL plasma, equations (1)–(4) were solved by using numerical schemes discussed in *Kakad et al.* [2013]. The fluid simulation was performed in a one-dimensional system with periodic boundary conditions. We considered a realistic ion-to-electron mass ratio, m_i/m_e = 1836. Other input parameters for the simulation run are given in

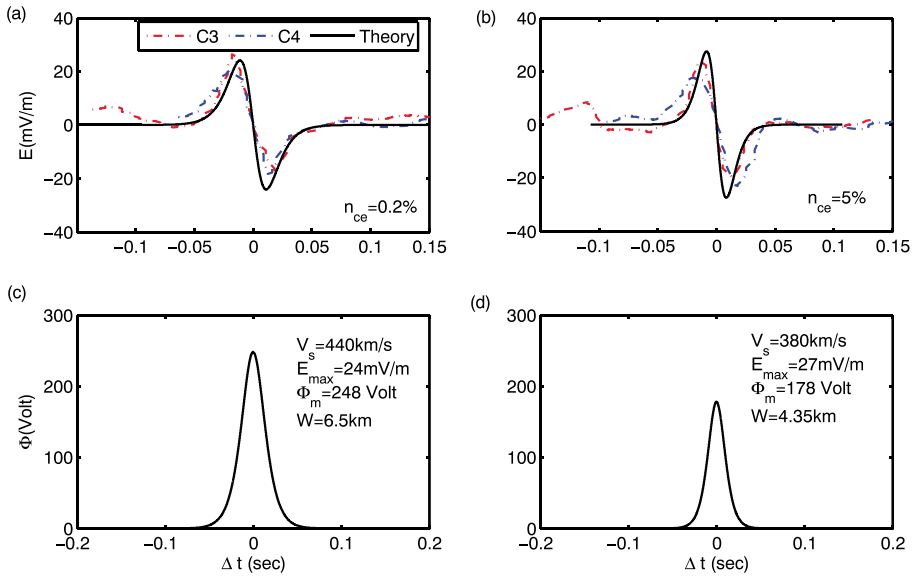

Figure 9. Comparison of the bipolar electric field structures obtained from theory with those in the spacecraft observations: (a) Obs. 3 and (b) Obs. 4. (c and d) The electrostatic potentials of the pulses.

Table 2. Initially, the background electron and ion densities were superimposed by considering the following localized Gaussian-type perturbation:

$$\delta n = \Delta n \exp\left(-\frac{(x-x_c)^2}{l_0^2}\right) \tag{11}$$

Here Δn and l_0 denote the amplitude and width of the superimposed density perturbations and x_c is the center of the simulation system. Thus, the perturbed densities $n_j(x) = n_{j0} + \delta n$ take the following form initially:

$$n_j(x) = n_{j0} + \Delta n \exp\left(-\frac{(x-x_c)^2}{l_0^2}\right) \tag{12}$$

The width and amplitude of the initial perturbation affect the characteristics of resultant solitary waves [*Kakad et al.*, 2013]. Such perturbations can originate in the EarthŠs magnetospheric regions by solar wind variations. We performed a simulation run with a density perturbation (Δn) of 0.04 for $n_{ce} = 5\%$ and 3.5%. Furthermore, we set the following parameter values in the fluid simulation run: grid spacing $\Delta x = 0.1\lambda_{di}$, time interval $\Delta t = 4 \times 10^{-5}\omega pi^{-1}$, system length $L_x = 512\lambda_{di}$, and $l_0 = 4\lambda_{di}$. We examined the evolution and propagation of different wave structures on the basis of the spatial and temporal evolution of their potential (ϕ_r, the unnormalized potential) and the electric field (E_r, the unnormalized electric field) for both cases, which are depicted in Figures 10a (for $n_{ce} = 5\%$) and 10b (for $n_{ce} = 3.5\%$). Here $x = 0$ represents the center of the simulation system. The spatial and temporal evolution of the electrostatic potential (ϕ_r) shows the presence of slow ion acoustic (curves 1 and 4), fast ion acoustic (curves 2 and 5), and electron acoustic modes (curves 3 and 6) propagating toward the left side and right side boundaries of the simulation system, in agreement with the predictions of the nonlinear fluid theory. Here structures propagating toward the right side boundary are

Table 2. Normalized Parameters Used in the Fluid Simulation of Obs. 4[a]

Simulation Parameter	Cold Electrons	Hot Electrons	Cold Ions	Hot Ions
Density (n_j)	0.05	0.95	0.46	0.54
Drift velocity (v_j)	−0.538	1.256	−0.021	0.629
Thermal velocity (V_{tj})	5.1674	26.735	0.0988	1
Mass	1	1	1/1836	1/1836

[a]The drift velocities are normalized by the hot ion thermal velocity.

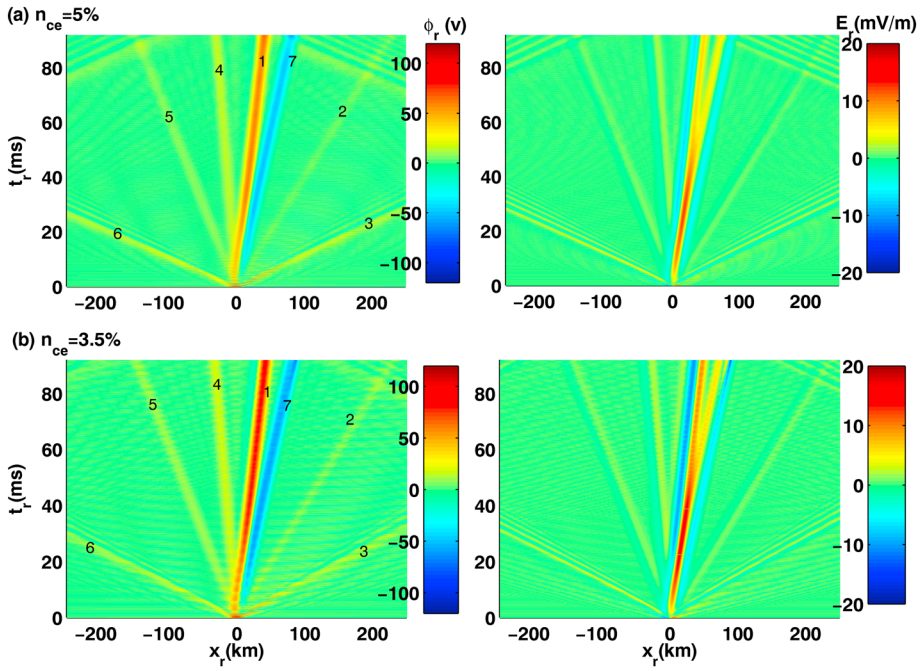

Figure 10. Spatial and temporal evolution of the electrostatic potential (ϕ_r) in the fluid simulation of the PSBL parameters (Obs. 4) for (a) $n_{ce} = 5\%$ and (b) $n_{ce} = 3.5\%$. The fluid simulation shows the coexistence of the slow ion acoustic modes (curves 1 and 4), fast ion acoustic modes (curves 2 and 5), electron acoustic modes (curves 3 and 6), and Buneman mode (curve 7). The positive *x* axis direction is the earthward direction, whereas the negative *x* axis direction is directed tailward. The distinct wave structures, seen ahead of the electron acoustic waves, represent the Langmuir wave.

moving earthward. The fluid simulation reveals the presence of an extra mode (curve 7) that is propagating in the positive *x* direction with a phase speed between those of slow and fast ion acoustic modes in both cases. This mode has potential structures with a negative polarity and is associated with the Buneman instability, which occurs because of relative drift between ion and electron populations present in the PSBL region. The simulation also shows the propagation of the Langmuir mode ahead of the electron acoustic mode in the simulation system.

The presence of the slow and fast ion acoustic modes, electron acoustic mode, Buneman mode, and Langmuir mode in the simulations is confirmed from the dispersion diagram. The $\omega - k$ diagram obtained by Fourier transforming the electric field in space and time for a period $\omega_{pi}t = 80$ is shown in Figure 11 (for $n_{ce} = 5\%$). The lowermost dispersion curves 1 and 4 represent slow ion acoustic modes, curves 2 and 5 denote fast ion acoustic modes, and curves 3 and 6 represent electron acoustic waves. Curve 7 represents the Buneman mode. The dispersion curve of the Langmuir waves is not shown in Figure 11 as we have restricted the *y* axis limit to 7. The dash-dotted black lines in Figure 11 show the average speed of each mode, which is obtained from the spatial and temporal variations of the mode (Figure 10a). The slopes of the curves also confirm the identity of the modes.

We calculated the normalized phase speed (Mach number) of each mode in the fluid simulation, for comparison with that predicted by theory for $n_{ce} = 5\%$. The normalized drift speeds obtained from the simulation (theory) for wave modes 1 to 6 in Figure 10a are 0.67, 2.48, 12.43, −0.51, −1.30, and −14.10 (0.47, 2.44, 13.15, −0.50, −1.20, and −14.04). Clearly, the normalized speeds of the slow and fast ion acoustic modes and the electron acoustic modes obtained from the fluid simulation are comparable with those predicted by theory. The normalized speed of the structure associated with the Buneman instability was found to be 1.298, which is greater than the hot ion thermal velocity. In this case, the unnormalized electric field amplitude, width, and drift speed of the slow ion acoustic mode is found to be ∼6 mV/m, 5.9 km, and 449 km/s, respectively. The electric field in this case is comparatively less than the estimated value from the theory for Obs. 4. This is due to the transfer of the energy to the growing Buneman mode in the system. Furthermore, we performed simulation for $n_{ce} = 3.5\%$. The potential (ϕ_r) and the electric field (E_r) in this case are shown in Figure 10b. The electric field amplitude, width, and drift speed of the slow ion acoustic mode is found to be ∼10 mV/m, 6.2 km,

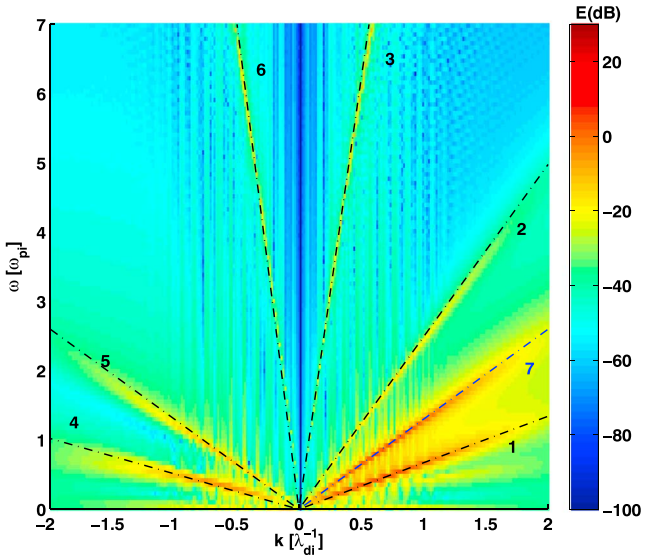

Figure 11. The $\omega - k$ dispersion diagram for $\omega_{pi}t = 100$ for Obs. 4 (for $n_{ce} = 5\%$). The dispersion diagram confirms the coexistence of the slow ion acoustic modes (curves 1 and 4), fast ion acoustic modes (curves 2 and 5), electron acoustic modes (curves 3 and 6), and Buneman mode (Curve 7). The speed of each mode, estimated from the slope of their spatiotemporal propagation, is shown by the slanted black dash-dotted lines. The dispersion curve of the Langmuir waves is not shown in this figure, as we have restricted the *y* axis limit to 7.

and 468 km/s, respectively. These characteristics are closed to the observations of the slow ESWs. The fluid simulation indicates that the nonlinear fluid theory overestimate the required cold electron density to model the slow ESW observation. This overestimation of the cold electron density might be due to the limitation of the nonlinear fluid theory that do not handle the Buneman instability in the analysis.

Figures 10 and 11 show that the propagation of slow and fast ion acoustic modes and electron acoustic modes is sustained in the presence of the moderate Buneman instability in the PSBL region. The fluid simulation showed that the Buneman mode propagated earthward with a negative potential of ~50 V (for $n_{ce} = 5\%$) and ~65 V (for $n_{ce} = 3.5\%$), whereas the slow ion acoustic mode propagating earthward had a potential of approximately ~55 V (for $n_{ce} = 5\%$) and ~85 V (for $n_{ce} = 3.5\%$). Hence, the simulation suggest that the slow ion acoustic mode can satisfactorily explain the characteristics of SESWs observed in PSBL region.

6. Discussion and Conclusions

We modeled an SESW event recorded by the C3 and C4 spacecraft at (−14, −4, 2) R_E (in GSM coordinates) in the Earth's magnetotail region. This SESW event was recently reported by *Norgren et al.* [2015a], and it was characterized by earthward propagating bipolar electric field pulses with a propagation speed of approximately 500 km/s and half widths of approximately $2–4\lambda_{De}$; the authors speculated that the event featured slow electron holes generated by a modified Buneman instability in the plasma. Recently, *Norgren et al.* [2015b] explained the generation of SESWs in a three-component plasma consisting of stationary ions, thermal stationary background electrons, and a relatively cold electron beam with a variable density and drift speed. Their model shows that at low beam speeds, the electron beam interacts with the ions, producing an instability akin to the Buneman instability and generating waves with a low speed. Furthermore, their linear theory of Buneman instability does not show any unstable mode for actually observed parameters in the magnetotail. However, when the electron beam temperature is reduced, their linear model shows the existence of an unstable electron-electron/electron-ion mode in the magnetotail. The assumption of an initially cold beam in their model was justified on the ground that the beam might have excited the instability and subsequent trapping of electrons, leading to the formation of SESWs earlier than the time of their observation by the Cluster spacecraft. These SESWs probably heated the electron beam, which is seen in the satellite observations of the SESWs in the magnetotail. However, it is not clear how much earlier the cold beam formed the phase space holes before they were observed as ESWs by the C3 and C4 spacecraft and for how long these phase space holes survive.

On the other hand, our model simulates the magnetotail observations of electron and ion distributions during or close to the time of SESW observations by Cluster spacecraft on 31 August 2007. We analyze the PEACE electron data and CIS (HIA) ion data for the interval 10:17:37 to 10:17:58 when the SESWs were observed in the magnetotail (see Table 1). When the parameters in Table 1 are used as input, the nonlinear model supports bipolar electric field structures associated with the slow and fast ion acoustic solitary waves and the electron acoustic waves simultaneously. In particular, the slow ion acoustic solitary wave speed obtained from the model is always less than 500 km/s. The theoretical estimates of the speeds, widths, and the amplitudes associated with the slow ion acoustic solitary waves are consistent with the observed values of the SESWs.

We studied the evolution of SESWs in the PSBL region through a one-dimensional fluid code with a realistic ion-to-electron mass ratio. Our fluid simulation confirmed the presence of slow and fast ion acoustic modes, an electron acoustic mode, and an extra Buneman mode in the Earth's PSBL region. While the results obtained from theory and the simulation are comparable, a new mode, attributed to the Buneman instability, is seen in the simulation. However, the Buneman mode cannot explain the observed SESWs as it is associated with a relatively higher speed and negative wave potentials. Our simulation shows that the earthward propagating slow ion acoustic mode can be sustained in the presence of the Buneman instability. Thus, the present study supports the view that the SESWs in the PSBL region can be interpreted as slow ion acoustic solitary waves.

It is possible to have in situ observations of solitary structures associated with both slow ion acoustic mode and the Buneman instability in the PSBL. We have looked into the electric field data from both Cluster-3 and Cluster-4 spacecraft during the SESW event. However, most of the structures in the data are identified as the positive amplitude slow ion acoustic mode during the time interval of the ESWs. We do not see any clear evidence of the negative amplitude structures associated with the Buneman mode in the observed electric field data for this particular event. One plausible reason for not detecting the Buneman mode by the spacecraft may be due to the shorter time scale of the structure associated with the unstable Buneman mode in comparison with the time scale of the structure associated with the stable ion acoustic mode. The detailed investigation of the in situ simultaneous observations of both slow ion acoustic solitary waves and the Buneman mode in the PSBL is left as future studies.

Acknowledgments
We thank the Cluster Principal Investigator teams and the Cluster Science Archive (http://www.cosmos.esa.int/web/csa) for providing the data used in this study. This study was supported by an Indo-Japanese bilateral research project. The model computations were performed on the High Performance Computing System at the Indian Institute of Geomagnetism. G.S.L. thanks the National Academy of Sciences, India, for support under the NASI-Senior Scientist Platinum Jubilee Fellowship.

References

Bale, S. D., P. J. Kellogg, D. E. Larsen, R. P. Lin, K. Goetz, and R. P. Lepping (1998), Bipolar electrostatic structures in the shock transition region: Evidence of electron phase space holes, *Geophys. Res. Lett.*, *25*(15), 2929–2932, doi:10.1029/98GL02111.

Bernstein, I. B., J. M. Greene, and M. D. Kruskal (1957), Exact nonlinear plasma oscillations, *Phys. Rev.*, *108*, 546–550, doi:10.1103/PhysRev.108.546.

Berthomier, M., R. Pottelette, and M. Malingre (1998), Solitary waves and weak double layers in a two-electron temperature auroral plasma, *J. Geophys. Res.*, *103*(A3), 4261–4270, doi:10.1029/97JA00338.

Cattell, C. A., J. Dombeck, J. R. Wygant, M. K. Hudson, F. S. Mozer, M. A. Temerin, W. K. Peterson, C. A. Kletzing, C. T. Russell, and R. F. Pfaff (1999), Comparisons of polar satellite observations of solitary wave velocities in the plasma sheet boundary and the high altitude cusp to those in the auroral zone, *Geophys. Res. Lett.*, *26*(3), 425–428, doi:10.1029/1998GL900304.

Cattell, C. A., J. Crumley, J. Dombeck, J. R. Wygant, and F. S. Mozer (2002), Polar observations of solitary waves at the Earth's magnetopause, *Geophys. Res. Lett.*, *29*(5), 91–94, doi:10.1029/2001GL014046.

Chen, L.-J., D. J. Thouless, and J.-M. Tang (2004), Bernstein-Greene-Kruskal solitary waves in three-dimensional magnetized plasma, *Phys. Rev. E*, *69*, 55401, doi:10.1103/PhysRevE.69.055401.

Dubouloz, N., R. A. Treumann, R. Pottelette, and M. Malingre (1993), Turbulence generated by a gas of electron acoustic solitons, *J. Geophys. Res.*, *98*(A10), 17,415–17,422, doi:10.1029/93JA01611.

Ergun, R. E., et al. (1998), Fast satellite observations of large-amplitude solitary structures, *Geophys. Res. Lett.*, *25*(12), 2041–2044, doi:10.1029/98GL00636.

Fox, W., M. Porkolab, J. Egedal, N. Katz, and A. Le (2012), Observations of electron phase-space holes driven during magnetic reconnection in a laboratory plasma, *Phys. Plasmas*, *19*(3), 32118, doi:10.1063/1.3692224.

Franz, J. R., P. M. Kintner, and J. S. Pickett (1998), Polar observations of coherent electric field structures, *Geophys. Res. Lett.*, *25*(8), 1277–1280, doi:10.1029/98GL50870.

Goldman, M. V., M. M. Oppenheim, and D. L. Newman (1999), Nonlinear two-stream instabilities as an explanation for auroral bipolar wave structures, *Geophys. Res. Lett.*, *26*(13), 1821–1824, doi:10.1029/1999GL900435.

Gustafsson, G., et al. (1997), The electric field and wave experiment for the Cluster mission, in *The Cluster and Phoenix Missions*, edited by C. Escoubet, C. Russell, and R. Schmidt, pp. 137–156, Springer, Netherlands, doi:10.1007/978-94-011-5666-0-6.

Johnstone, A., et al. (1997), Peace: A Plasma Electron and Current Experiment, *Space Sci. Rev.*, *79*(1–2), 351–398, doi:10.1023/A:1004938001388.

Kakad, A., Y. Omura, and B. Kakad (2013), Experimental evidence of ion acoustic soliton chain formation and validation of nonlinear fluid theory, *Phys. Plasmas*, *20*(6), 62103, doi:10.1063/1.4810794.

Kakad, A. P., S. V. Singh, R. V. Reddy, G. S. Lakhina, S. G. Tagare, and F. Verheest (2007), Generation mechanism for electron acoustic solitary waves, *Phys. Plasmas*, *14*(5), 52305, doi:10.1063/1.2732176.

Kakad, B., A. Kakad, and Y. Omura (2014), Nonlinear evolution of ion acoustic solitary waves in space plasmas: Fluid and particle-in-cell simulations, *J. Geophys. Res. Space Physics*, *119*, 5589–5599, doi:10.1002/2014JA019798.

Kojima, H., et al. (1994), Relation between electrostatic solitary waves and hot plasma flow in the plasma sheet boundary layer: Geotail observations, *Geophys. Res. Lett.*, *21*(25), 2919–2922, doi:10.1029/94GL02111.
Lakhina, G. S., A. P. Kakad, S. V. Singh, and F. Verheest (2008a), Ion- and electron-acoustic solitons in two-electron temperature space plasmas, *Phys. Plasmas*, *15*(6), 62903, doi:10.1063/1.2930469.
Lakhina, G. S., S. V. Singh, A. P. Kakad, F. Verheest, and R. Bharuthram (2008b), Study of nonlinear ion- and electron-acoustic waves in multi-component space plasmas, *Nonlinear Process. Geophys.*, *15*(6), 903–913, doi:10.5194/npg-15-903-2008.
Lakhina, G. S., S. V. Singh, A. P. Kakad, M. L. Goldstein, A. F. Viñas, and J. S. Pickett (2009), A mechanism for electrostatic solitary structures in the Earth's magnetosheath, *J. Geophys. Res.*, *114*, A09212, doi:10.1029/2009JA014306.
Lakhina, G. S., S. V. Singh, A. P. Kakad, and J. S. Pickett (2011), Generation of electrostatic solitary waves in the plasma sheet boundary layer, *J. Geophys. Res.*, *116*, A10218, doi:10.1029/2011JA016700.
Lefebvre, B., L.-J. Chen, W. Gekelman, P. Kintner, J. Pickett, P. Pribyl, S. Vincena, F. Chiang, and J. Judy (2010), Laboratory measurements of electrostatic solitary structures generated by beam injection, *Phys. Rev. Lett.*, *105*, 115001, doi:10.1103/Phys.Rev.Lett.105.115001.
Lefebvre, B., L.-J. Chen, W. Gekelman, P. Kintner, J. Pickett, P. Pribyl, and S. Vincena (2011), Debye-scale solitary structures measured in a beam-plasma laboratory experiment, *Nonlinear Process. Geophys.*, *18*, 41–47, doi:10.5194/npg-l8-41-2011.
Li, S., S. Zhang, H. Cai, and S. Yu (2014), Concentration of electrostatic solitary waves around magnetic nulls within magnetic reconnection diffusion region: Single-event-based statistics, *Earth Planets Space*, *66*(1), 161, doi:10.1186/s40623-014-0161-3.
Malaspina, D. M., D. L. Newman, L. B. Willson, K. Goetz, P. J. Kellogg, and K. Kerstin (2013), Electrostatic solitary waves in the solar wind: Evidence for instability at solar wind current sheets, *J. Geophys. Res. Space Physics*, *118*, 591–599, doi:10.1002/jgra.50102.
Mangeney, A., C. Salem, C. Lacombe, J.-L. Bougeret, C. Perche, R. Manning, P. Kellogg, K. Goetz, S. Monson, and J.-M. Bosqued (1999), Wind observations of coherent electrostatic waves in the solar wind, *Ann. Geophys.*, *17*(3), 307–320, doi:10.1007/s00585-999-0307-y.
Matsumoto, H., H. Kojima, T. Miyatake, Y. Omura, M. Okada, I. Nagano, and M. Tsutui (1994), Electrostatic solitary waves (ESW) in the magnetotail: BEN wave forms observed by GEOTAIL, *Geophys. Res. Lett.*, *21*(25), 2915–2918, doi:10.1029/94GL01284.
Matsumoto, H., X. H. Deng, H. Kojima, and R. R. Anderson (2003), Observation of electrostatic solitary waves associated with reconnection on the dayside magnetopause boundary, *Geophys. Res. Lett.*, *30*(6), 1326, doi:10.1029/2002GL016319.
Norgren, C., A. Vaivads, Y. V. Khotyaintsev, and M. Andre (2012), Lower hybrid drift waves: Space observations, *Phys. Rev. Lett.*, *109*, 55001, doi:10.1103/PhysRevLett.109.055001.
Norgren, C., M. André, A. Vaivads, and Y. V. Khotyaintsev (2015a), Slow electron phase space holes: Magnetotail observations, *Geophys. Res. Lett.*, *42*, 1654–1661, doi:10.1002/2015GL063218.
Norgren, C., M. André, D. B. Graham, Y. V. Khotyaintsev, and A. Vaivads (2015b), Slow electron holes in multicomponent plasmas, *Geophys. Res. Lett.*, *42*, 7264–7272, doi:10.1002/2015GL065390.
Olivier, C. P., S. K. Maharaj, and R. Bharuthram (2015), Ion-acoustic solitons, double layers and supersolitons in a plasma with two ion- and two electron species, *Phys. Plasmas*, *22*(8), 82312, doi:10.1063/1.4928884.
Omura, Y., H. Matsumoto, T. Miyake, and H. Kojima (1996), Electron beam instabilities as generation mechanism of electrostatic solitary waves in the magnetotail, *J. Geophys. Res.*, *101*(A2), 2685–2697, doi:10.1029/95JA03145.
Paschmann, G., A. N. Fazakerley, and S. J. Schwartz (1998), Moments of plasma velocity distributions, in *Analysis Methods for Multi-Spacecraft Data*, vol. 1, edited by G. Paschmann and P. W. Daly, pp. 125–157, ISSI Sci. Rep. Ser., ESA/ISSI.
Pickett, J. S., L.-J. Chen, S. W. Kahler, O. Santolík, D. A. Gurnett, B. T. Tsurutani, and A. Balogh (2004), Isolated electrostatic structures observed throughout the Cluster orbit: Relationship to magnetic field strength, *Ann. Geophys.*, *22*(7), 2515–2523, doi:10.5194/angeo-22-2515-2004.
Pickett, J. S., et al. (2005), On the generation of solitary waves observed by Cluster in the near-Earth magnetosheath, *Nonlinear Process. Geophys.*, *12*(2), 181–193, doi:10.5194/npg-12-181-2005.
Pickett, J. S., et al. (2009), Electrostatic solitary waves in current layers: From Cluster observations during a super-substorm to beam experiments at the LAPD, *Nonlinear Process. Geophys.*, *16*(3), 431–442, doi:10.5194/npg-16-431-2009.
Réme, H., et al. (1997), The Cluster Ion Spectrometry (CIS) experiment, in *The Cluster and Phoenix Missions*, edited by C. Escoubet, C. Russell, and R. Schmidt, pp. 303–350, Springer, Netherlands, doi:10.1007/978-94-011-5666-0-12.
Verheest, F., T. Cattaert, G. Lakhina, and S. Singh (2004), Gas-dynamic description of electrostatic solitons, *J. Plasma Phys.*, *70*(2), 237–250.
Wilson, L. B., C. A. Cattell, P. J. Kellogg, K. Goetz, K. Kersten, J. C. Kasper, A. Szabo, and M. Wilber (2010), Large-amplitude electrostatic waves observed at a supercritical interplanetary shock, *J. Geophys. Res.*, *115*, A12104, doi:10.1029/2010JA015332.